PROCEEDINGS OF SPIE

SPIEDigitalLibrary.org/conference-proceedings-of-spie

Current limitation of the THD2 bench: the scatter issue

A. Potier, P. Baudoz, R. Galicher, F. Patru, S. Thijs

A. Potier, P. Baudoz, R. Galicher, F. Patru, S. Thijs, "Current limitation of the THD2 bench: the scatter issue," Proc. SPIE 10698, Space Telescopes and Instrumentation 2018: Optical, Infrared, and Millimeter Wave, 106986G (21 August 2018); doi: 10.1117/12.2313986

SPIE.

Event: SPIE Astronomical Telescopes + Instrumentation, 2018, Austin, Texas, United States

Current limitation of the THD2 bench : the scatter issue.

A. Potier[a], P. Baudoz[a], R. Galicher[a], F. Patru[a], S. Thijs[a]

[a] LESIA, Observatoire de Paris, Université PSL, CNRS, Univ. Paris Diderot, Sorbonne Université, Sorbonne Paris Cité, 5 place Jules Janssen, 92195 Meudon, France

ABSTRACT

Direct imaging is crucial to increase our knowledge on extrasolar planetary systems. It can detect long orbits planets that are inaccessible by other methods and it allows the spectroscopic characterization of exoplanet's athmospheres. During the past few years, several giant planets were detected by direct imaging methods. Yet, as exoplanets are 10^3 to 10^{10} fainter than their host star in visible and near-infrared wavelengths, direct imaging requires extremely high contrast imaging techniques, especially to detect low-mass and mature exoplanets. Coronagraphs are used to reject the diffracted light of an observed star and obtain images of its circumstellar environment. Nevertheless, coronagraphs are efficient only if the wavefront is flat because aberrated wavefronts induce speckles in the focal plane which mask exoplanet images. Thus, wavefront sensors associated to deformable mirrors are mandatory to correct speckles by reducing aberrations. To test coronagraph techniques and focal plane wavefront sensors at very high contrast level, we developed the THD2 bench in the optical wavelengths. On the THD2 bench, we routinely reach 10^{-8} raw contrast level inside the dark hole over broadbands but this level is not sufficient to detect low-mass exoplanets. At this level, it seems that many experimental factors can affect the contrast and understanding which one is limiting the final detection contrast will be useful to upgrade the THD2 bench and to develop the next generation of space-based instruments (LUVOIR, HabEx) aiming to reach 10^{-10} contrast level. We started a complete study of the instrumental limitations of the THD2 bench, focusing on scattering which could add intensity on the detector or polarization effects and residual laboratory turbulences. In this paper, we present the methods used to estimate the amount of scattered light that reaches the final detector on the THD2 bench.

Keywords: Exoplanets, High Contrast Imaging, Wavefront Sensor, Scattering

1. INTRODUCTION

Direct imaging techniques are crucial to discover more exoplanets and to probe their atmospheres. Nevertheless, an exoplanet is 10^3 to 10^{10} fainter than its hosting star in visible and near-infrared wavelength at a fraction of arcsecond which explain why only a dozen of warm and massive exoplanets where detected by direct imaging. That technique requires large telescopes and the use of coronagraph to reject the diffracted light of an observed star and reveal the light from the exoplanet in the circumstellar environment. Yet, a coronagraph is efficient if the wavefront is perfectly flat because an aberatted wavefront induces speckles in the image which prevent to detect exoplanets. Even in space, small quasi-static aberrations need to be reduced thanks to a wavefront control loop device composed mainly with a wavefront sensor in the focal plane and deformable mirrors to make the wavefront flatter. In order to reach 10^{-10} contrast level on the next generation of space-based instruments aiming to detect earth-like exoplanets, we developed at LESIA, Observatoire de Paris a test bench for wavefront sensing in the focal plane where we manage to routinely reach 10^{-8} raw contrast level [1][2]. This bench, called THD2 (Très Haute Dynamique in french) works in visible light (550nm to 900nm). As shown in Figure 1, the laser source goes through 6 Off-Axis Parabolae (OAP) because the one named "Parabola" is settled twice on the optical path. The testbench is also composed with three deformable mirrors and one Tip-Tilt mirror [3][4]. Eventually, the final detector is a NEO sCMOS camera with 6.5μm$\times 6.5\mu$m pixel area and with a total dimension of 14.0mm$\times$14.0mm. That final detector samples the final image in order to get around 8 pixels per resolution element (lambda/D).

In order to dig deeper in term of contrast in that final detector, we need to understand the different limitations of the THD2 and we found out three main effects which could limit the THD2 bench: scattering on reflectors, polarization effects or an unstability effect due to temperature change. We will focus in this document on reflectors scatter limitation.

Further author information: Send correspondence to axel.potier@obspm.fr or pierre.baudoz@obspm.fr

Space Telescopes and Instrumentation 2018: Optical, Infrared, and Millimeter Wave, edited by Makenzie Lystrup, Howard A. MacEwen, Giovanni G. Fazio, Proc. of SPIE Vol. 10698, 106986G
 · doi: 10.1117/12.2313986

Indeed, the algorithms developped on the THD2 need coherent light coming from the source whereas reflectors scattering due to surfaces defect could carry incoherent light through the bench which is not minimized by the wavefront control loop. Those defects are caused by surfaces scratch, dust deposit on mirror surfaces and microroughness created during mirrors manufacturing or reflecting treatment of mirrors. In Section 2.2, we plot the amount of scattered light measured using the experiment setup explained in Section 2.1. We then describe a model in Section 3.1 that we use to calculate scattering level induced by microroughness for one reflector. Using microroughness measurements (section 3.2), we simulate the contrast limit sets by this defect in the final detector (section 3.3).

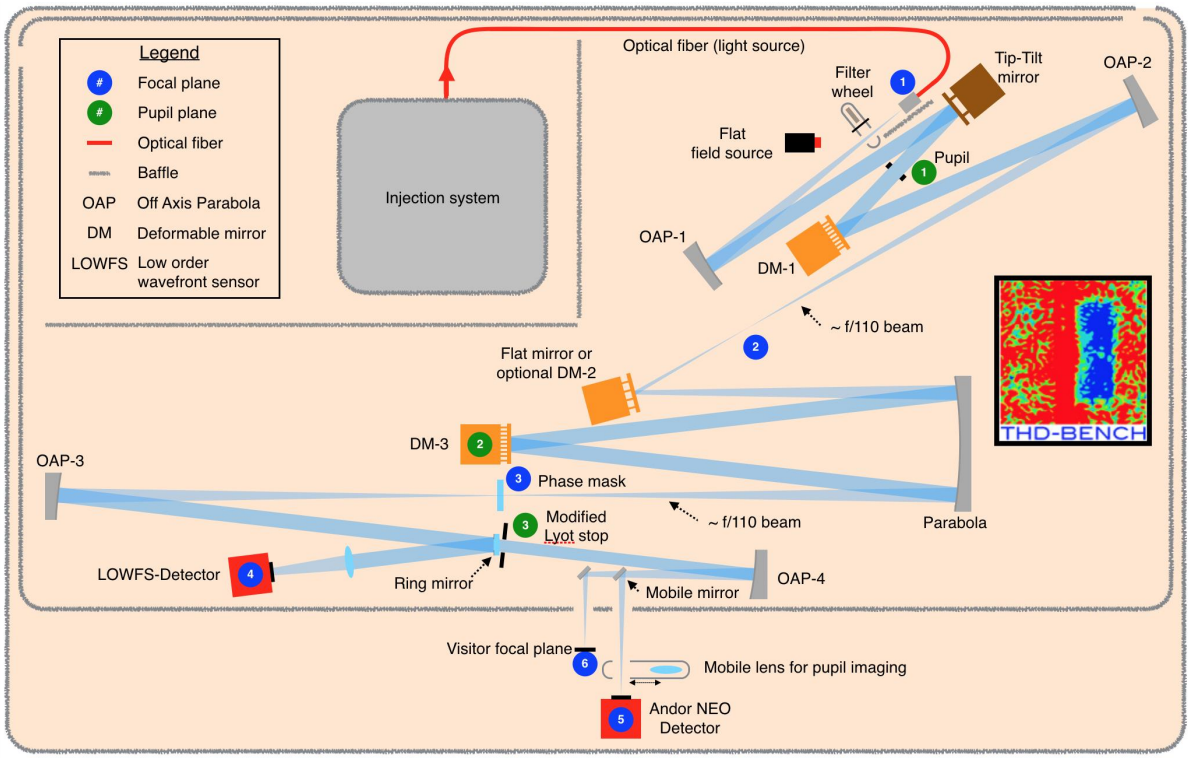

Figure 1: THD2 bench design.

2. SURFACE SCATTER MEASUREMENTS

2.1 Experimental setup

In order to estimate the level of scattered light by both microroughness and dust deposit on all surface reflectors of the THD2, we radiated an OAP similar to those used on the test bench with a bright and collimated laser source in order to estimate the scattered light for different angles and wavelengths. We used a Manta camera manufactured by AVT to get the scattered flux outside the specular beam, reflected by the OAP. The Manta camera and the OAP were fixed together so that the camera and its associate lens stay parallel to the AOP surface tangent. In that configuration, we could get the OAP's surface image on the detector; this image stays focused whatever the scattered measuring angle θ. The system {camera+OAP} can only rotate around the rotation axis P, settled on the OAP's center as shown in Figure 2, Left. This rotation allows to bring closer or to take away the specular beam from the camera, thus a decreasing or an increasing of the θ angle respectively.

The image in Figure 2, on the right shows the camera images taken for 12°, 20° and 35° incident angles which correspond to the same measuring angles θ. We can first observe that the radiated OAP area increases with θ due to the incident angle variation during the rotation around P axis. We assume that scatter is shift invariant: diffusion pattern is independant of the incident beam and there is no difference between backward and forward scattering (diffusion pattern

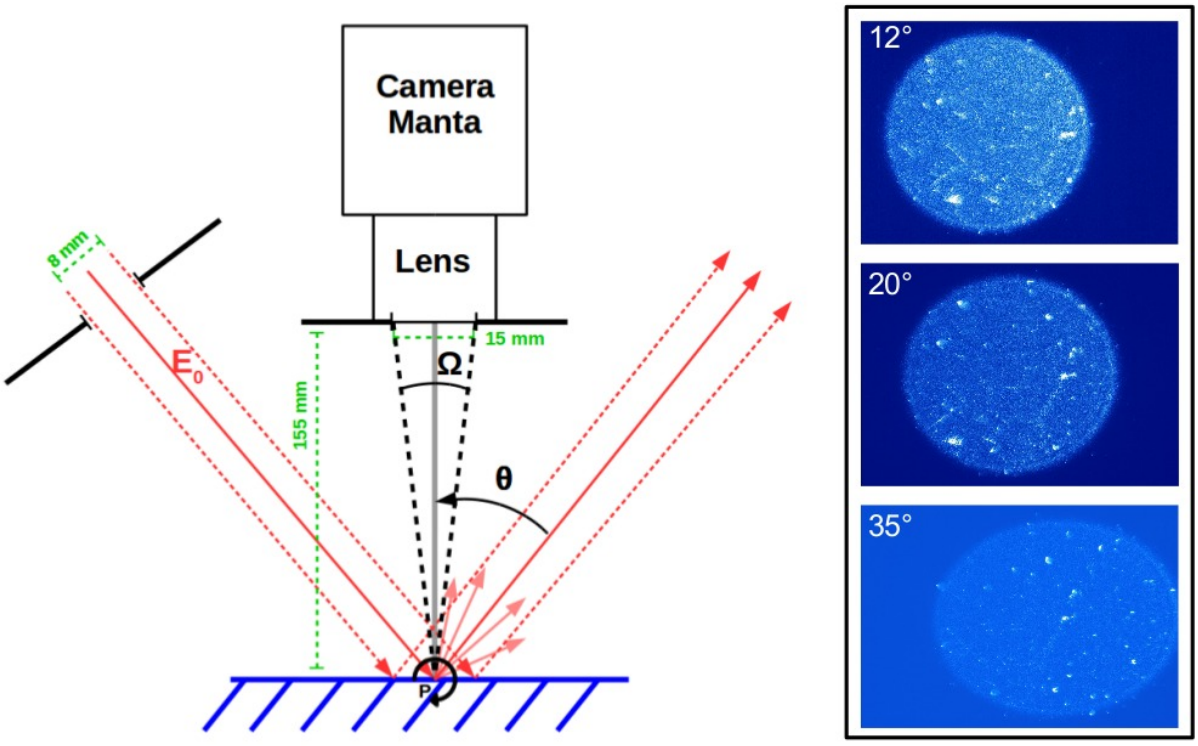

Figure 2: Left: Experiment scheme for measuring the amount of intensity scattered. The system Manta camera and mirror is fixed together and can only rotate around the rotating axis P, varying the scattered angle θ from the specular beam. Right: Images taken for a wavelength of 640nm at 12, 20 and 35 degrees from the specular beam showing the scatter shape spreading along one direction.

is independent from θ being positive or negative). Our experiment only allows to measure the backward scattering. Moreover, we assume the surface is isotropic and homogeneous: the reflectance and the microroughness and dust distributions are constant over the entire surface. The image in Figure 2, on the right shows the two causes of scattering: the elliptic spot whose shape corresponds to the projection of the incident beam on the surface mirror comes from microroughness whereas local intensity peaks are due to mirror surface contamination by dust deposit and scratch.

2.2 Defining and measuring the Bidirectional Reflectance Distribution Function (BRDF)

One experimental quantity is relevant to measure the level of scattered intensity for an optical component: it is the Bidirectional Reflectance Distribution Function [5] (BRDF), which measures the fraction of scattered radiation into a given projected solid angle and defined as, in steradians^{-1}:

$$BRDF(\theta) = \frac{Ls(\theta)}{E_o \cdot \Omega} \tag{1}$$

where $L_s(\theta)$ is the scattered intensity measured on the detector settled at a θ angle position from the scatter beam and covering a solid angle Ω. Here, we measure $L_s(\theta)$ summing the intensity of all the pixels occupied by the incident beam footprint (Figure 2, on the right). As we associate a 15mm diaphragm to the Manta camera and as the detector is placed at 155mm from the AOP surface, the solid angle to consider here is thus $\Omega = 0.0074$ sr. Eventually, E_o is the incident laser intensity impacting the OAP. We measured it initially, installing the detector directly in the specular beam. Thanks to all these different parameters, we are able to plot the BRDF curve for different θ angles (Figure 3). We thus notice that the scattering level decreases when the wavelength increases and the scattering level increases when we come closer to the specular beam. Yet, the purpose of this study is to measure the incoherent intensity due to scatter inside the specular beam, but the size of the camera prevents us to bring it closer to the specular beam and we cannot measure BRDF below

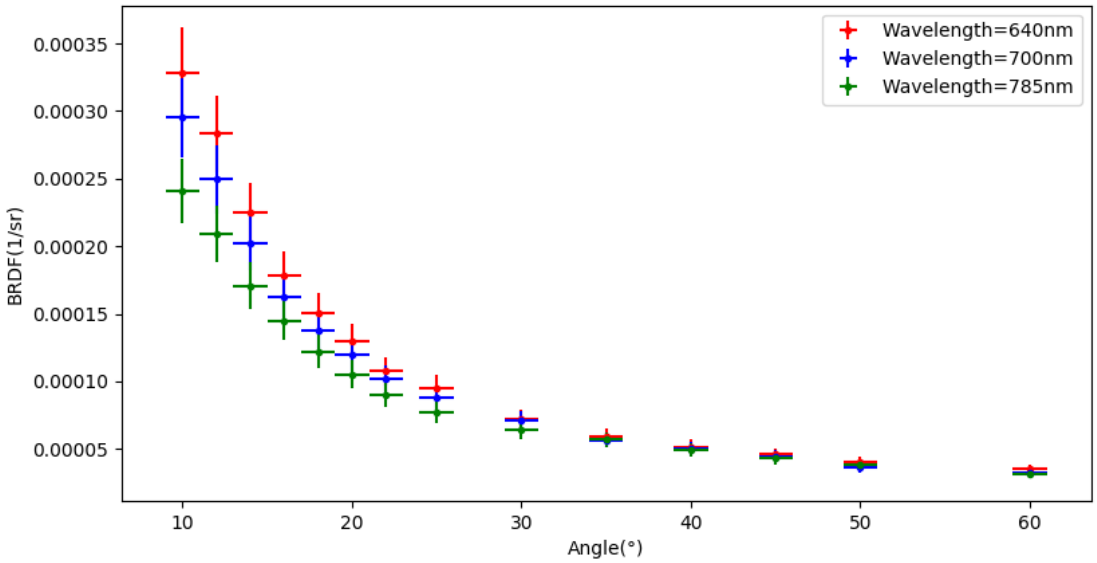

Figure 3: BRDF measured versus angle between the detector and the specular beam for three lasers with 640nm, 700nm and 785nm wavelength.

θ=10°. In order to estimate the parabola scattered intensity at narrow angles, some models propose a relationship between the BRDF and the OAP surface microroughness. Due to the instrument resolution limit (a pixel on the image in Figure 2 corresponds to a size of about 7.8μm), the experimental device does not allow us to measure the actual size of the particles stucked on the OAP's surface and we do not consider scattering by dust in the following part. Nevertheless, we are aware that dust can scatter light in the final detector on the THD2 bench [6] and this effect will be a part of a futur study. We will only consider microroughness effects in Section 3.

3. BRDF AND MICROROUGHNESS

3.1 Model of scatter light

The behaviour of a light scattered by a rough surface can be defined thanks to two statistical parameters as shown in Figure 4 [7][8]. The relevant specifications are the surface microrougness length distribution that we consider gaussian with a standard deviation σ_s, and the autocovariance function ACV which is unfortunately not gaussian in most of cases. The value of the autocovariance function at origin is equal to the squared standard deviation σ_s^2. Moreover, as the autocovariance Fourier transform is, by definition, equal to the Power Spectral Density (PSD), the area under the 2 Dimensional-PSD function is also equal to σ_s^2. We suppose next that the autocovariance function and the 2D-PSD function are axisymmetrics. Nevertheless, some spatial frequency do not have any optical effect. Indeed, spatial frequencies higher than $f_0 = \cos\theta/\lambda$ produce evanescent waves which do not impact the intensity scatter level impacting the final detector [7][8]. Thus, the relevent parameter σ_{rel} for optics has to be calculated thanks to the considered reflector's 2 Dimensional-PSD, and depends on the incident beam wavelength and on the incident angle:

$$\sigma_{rel}(\lambda,\theta) = \sqrt{2\pi \int_0^{\cos\theta/\lambda} \mathrm{PSD}(f) f\, df} \tag{2}$$

In 1976, Harvey developped a formula to study the scatter phenomena by modeling microroughness as an optical path length difference for photons impacting the considered reflector [7][8][9]. The reflector pupil function is thereby:

$$p_R(x,y) = \sqrt{R(x,y)} \cdot \exp[i4\pi \frac{h(x,y)}{\lambda}] \tag{3}$$

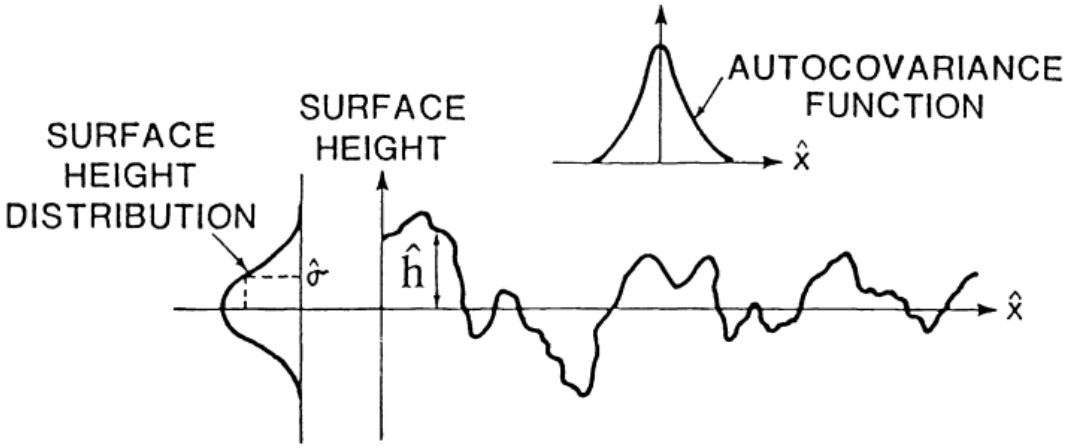

Figure 4: Surface height variations and relevant statistical parameters for a scatter study according to Harvey et al. [7][9]
.

where p_R is the reflector surface pupil function, $R(x, y)$ is its reflectivity and $h(x, y)$ represents the deviation of the surface height for the (x,y) position from the average surface height (Figure 4). By definition, the optical transfer function is the pupil normalized autocorrelation which brings about, in the case of our modified pupil function:

$$H_R(x, y) = \frac{\iint_{-\infty}^{+\infty} p_R(x', y') p_R^{\star}(x' - x, y' - y) dx' dy'}{\iint_{-\infty}^{+\infty} |p_R(x', y')|^2 dx' dy'} \tag{4}$$

Eventually, following the proposed calculation in the Harvey-Schack theory [9], the optical transfer function for our rough surface depends on the surface standard deviation and on the two dimensionnal autocovariance function ACV:

$$H_R(x, y) = \exp\left[-(4\pi\frac{\sigma_{rel}}{\lambda})^2(1 - \frac{\text{ACV}}{\sigma_s^2})\right] \tag{5}$$

The optical transfer function can be rewritten as the sum of a constant component A (which corresponds to the direct specular beam) and a gaussian component BQ(x,y) (which corresponds to the light scattered by the reflector):

$$H_R(x, y) = A + BQ(x, y) \tag{6}$$

where:

$$\begin{aligned} \text{A} &= \exp[-(4\pi\frac{\sigma_{rel}}{\lambda})^2] \\ \text{B} &= 1 - \exp[-(4\pi\frac{\sigma_{rel}}{\lambda})^2] \\ \text{Q}(x, y) &= \frac{\exp[(4\pi\sigma_{rel}/\lambda)^2 \text{ACV}/\sigma_s^2] - 1}{\exp[(4\pi\sigma_{rel}/\lambda)^2] - 1} \end{aligned} \tag{7}$$

The point spread function is defined as the Fourier transform of the optical transfer function which is the sum of 2 components (specular and scattered light). The point spread function becomes therefore a "Dirac" beam surrounded by a halo of scattered light which corresponds to the BRDF (Figure 5). In this study, we are interested in the BRDF at narrow angles. Yet, the BRDF calculated this way has to fit the former measures in Section 2.2 at larger angles.

3.2 From a power spectral density to a BRDF estimation

We first measured the power spectral density of our OAPs using a two dimensional interferometric profiler (Wyko NT9000) with a lateral resolution of 0.67 μm^2 and a depth precision of 0.1 nm. This gives us a PSD function between 0.001 and 1 μm^{-1} shown in Figure 6. Yet, we can observe a strong decrease of this curve for frequencies higher than 0.1μm^{-1} coming from the profiler resolution limit. Due to our instrument limits, we only consider the PSD between 0.01 and 0.1

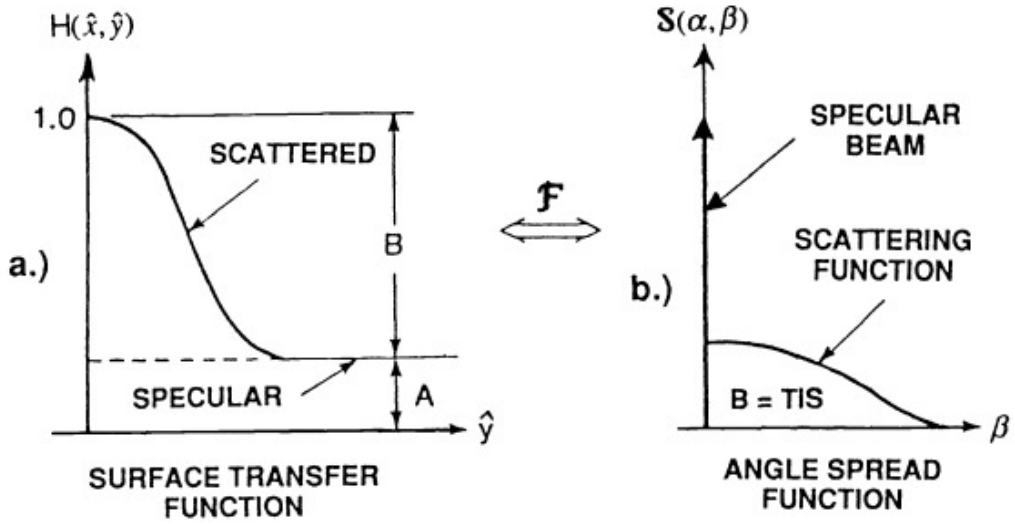

Figure 5: Optical transfer function and point spread function for a rough surface, according to Harvey et al. [7][9]

μm^{-1} to fit, with a least mean square regression, a function called 2D-$\mathcal{ABC}$, which is empirically the best representative of the real optical surfaces [10][11][12]:

$$\mathrm{PSD}(f)_{2D} = K\frac{\mathcal{AB}}{(1+(\mathcal{B}f)^2)^{(\mathcal{C}+1)/2}} \quad \text{where} \quad K = \frac{1}{2\sqrt{\pi}}\frac{\Gamma((\mathcal{C}+1)/2)}{\Gamma(\mathcal{C}/2)} \tag{8}$$

That function allows to reach a maximum equal to $(K \times \mathcal{A} \times \mathcal{B})$ for frequencies higher than $1/\mathcal{B}$ in order to avoid an infinite PSD function at zero spatial frequency, which is physically impossible. The $\mathcal{C}$+1 parameter corresponds to the PSD powerlaw falloff. We find $\mathcal{C} = 0.43 \pm 0.16$ (which means a PSD decrease in $f^{-1.43}$), which allows to directly calculate $\sigma_{rel} = (1.4 \pm 0.3) \times 10^{-9}$, integrating this 2D-$\mathcal{ABC}$ function in equation 2, from 0 to $1/\lambda$ (doing a Taylor developement limited for narrow angles, $\cos(\theta) \simeq 1$). Moreover, the 2D-$\mathcal{ABC}$ function owns an analytical Fourier transformed which

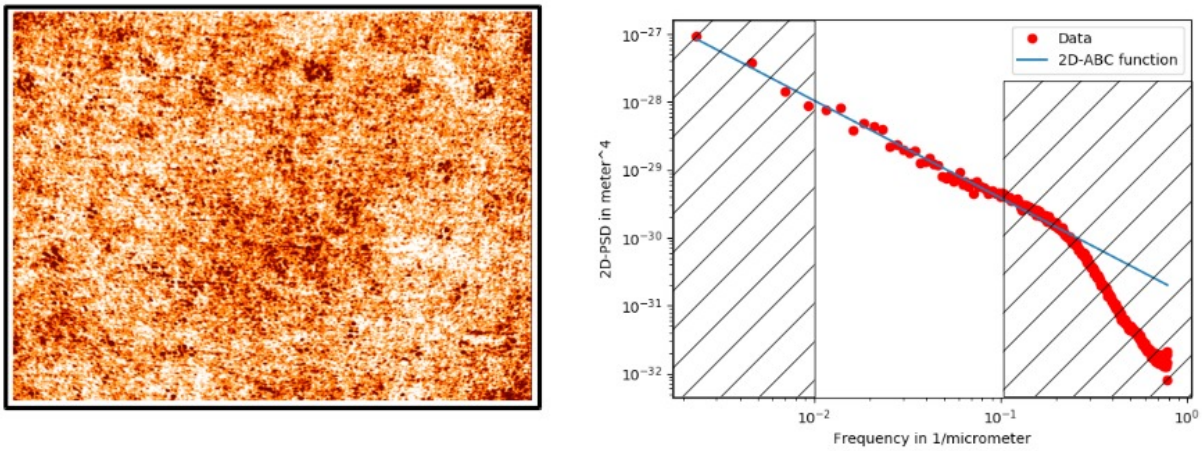

Figure 6: Left: OAP's Microroughness measuring by interferometric microscopy. Right: Measured PSD and fit with a 2D-$\mathcal{ABC}$ function.

allows to calculate the autocovariance function ACV [11]:

$$\mathrm{ACV}(r) = \sqrt{2\pi}\frac{\mathcal{A}}{\mathcal{B}}\frac{2^{-\mathcal{C}/2}}{\Gamma(\mathcal{C}/2)}\left(\frac{2\pi r}{\mathcal{B}}\right)^{(\mathcal{C}-1)/2}\mathcal{K}_{(\mathcal{C}-1)/2}\left(\frac{2\pi r}{\mathcal{B}}\right) \tag{9}$$

where $\mathcal{K}$ is the modified Bessel function of the second kind. Thus, we can insert the autocovariance function previously calculated in the equations 6 and 7 to find the BQ function. Eventually, we calculate the numerical Fourier transform of that two-dimensional BQ function and whose integral on the all hemisphere is normalized to be equal to the B parameter (which corresponds to the Total Integrated Scatter TIS and is equal to $\mathrm{TIS}_{\mathrm{microroughness}} = 5.2 \times 10^{-4}$ at 785nm). We thus get the scattered component of the point spread function which corresponds to the BRDF estimated from the OAP's microroughness measures (Figure 7). That Figure shows a consistency between the BRDF estimated in this Section and the BRDF experimentally measured in Section 2.2 at large angles. However, even if we find the same slope when we compare the estimated scatter and the measured scatter, we observe that we overestimate the estimated intensity scattered with a coefficient between 2 and 3 at large angles. Using this estimation, we apply it for all the reflectors of the THD2 bench in order to determine the total scatter level reaching our bench final detector.

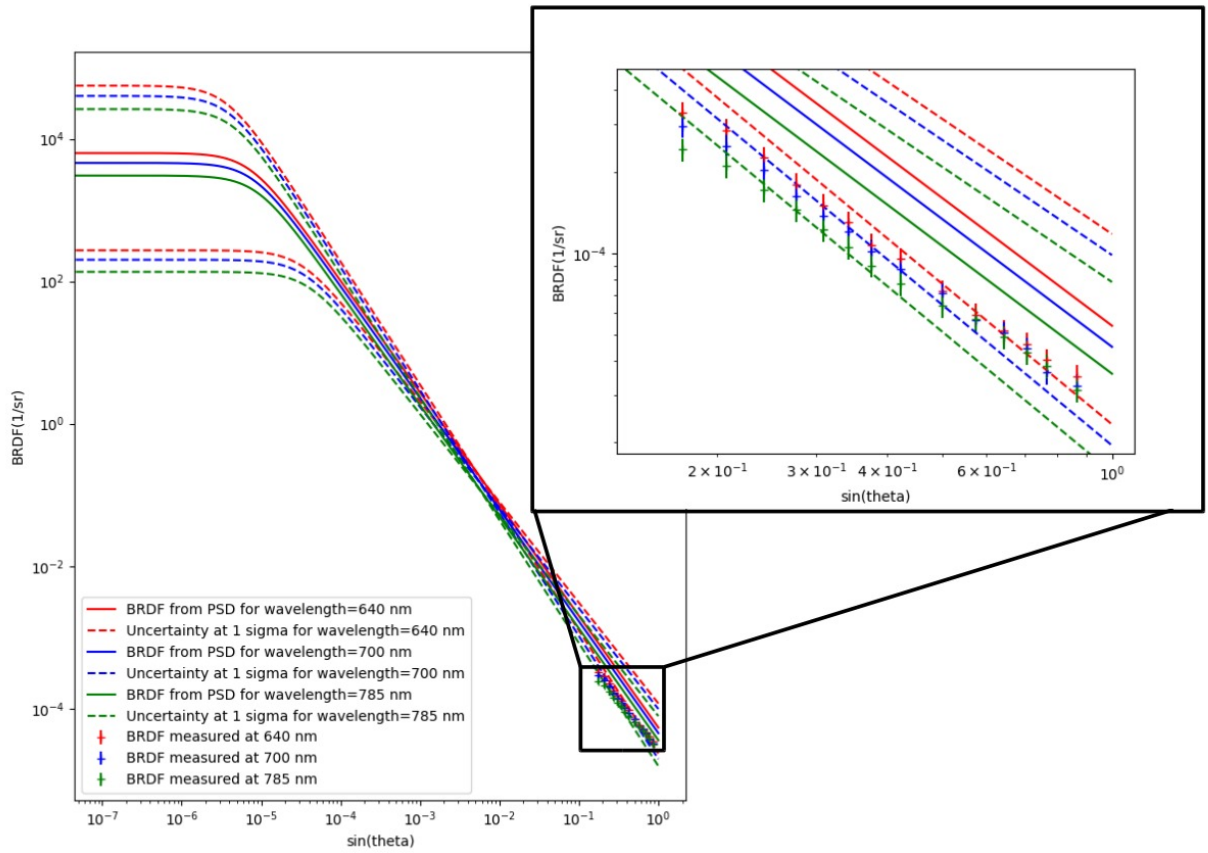

Figure 7: OAPs BRDF estimated from PSD (features) and directly measured (cross). The dashed lines correspond to the same BRDF estimation with a 1 sigma uncertainty on the $\mathcal{C}$ parameter.

3.3 Determining the microroughness intensity scattered level on the THD2 bench

Here, we look for determining the total level of scatter due to the 10 optical reflectors on the THD2 bench and really impacting the final detector. Thus, we have to determine the scatter solid angle in order to integrate the BRDF previously estimated in Section 3.2 for a relevent solid angle. We consider that the incident beam footprint is an axisymmetrical

extended object, and we split it in N concentric circles with a thick $\Delta r = R/N$ where R is the radius of the incident beam impacting the reflector and the ith circle from the center has an area of (for i going from 0 to $(N-1)$):

$$\Sigma(i) = (2i+1)\pi\Delta r^2 \tag{10}$$

We can therefore bring our study back to a sum of infinitesimal surfaces, each being located on the same radius, at a distance $(i+1/2)\Delta r$ from the extended object center, and for which we can determine the optical path through the test-bench thanks to geometrical optics. The optical path is limited by the different apertures of the THD2 bench, described in Table 1 and represented in green Figure 8. Thus, we can determine for each infinitesimal surfaces a scatter solid angle Ω_i which corresponds to a cone with a $2 \times \theta_i$ top angle. Each of these surfaces holding an initial energy of:

$$I_{ini}(i) = \frac{(2i+1)\pi\Delta r^2}{\pi R^2} E_0 \tag{11}$$

and considering a same BRDF function for all the THD2 bench reflectors (estimated Section 3.2), the intensity scattered hitting the detector and coming from that surface is therefore:

$$L_s(i) = \frac{(2i+1)}{N^2} E_0 \cdot 2\pi \int_{\lambda/D}^{\theta_i} (BRDF(\theta) \cdot \sin(\theta) \cdot d\theta) \tag{12}$$

with $BRDF$ the function estimated in Section 3.2 and E_0 the incident beam intensity. The lower limit of this integration is λ/D where D is the size of the beam radiating the reflector because structure whose size is higher than D are not radiated and therefore do not scatter. On Figure 8, the optical paths plotted in red represent the limit light rays for the infinitesimal scattering surface of OAP-1 and located at 4.5 mm from the reflector centre. We notice that some parts of the detector are not enlightenned by that scattering surface. Assuming the intensity scattered $L_s(i)$ for the ith surface is uniformly distributed on all the enlightenned pixels, the intensity scattered reaching the pixel (j,k) and coming from this surface is therefore:

$$I_{pix,i}(j,k) = \frac{1}{N_{pix}(i)} \cdot \frac{(2i+1)}{N^2} E_0 \cdot 2\pi \int_{\lambda/D}^{\theta_i} (BRDF(\theta) \cdot \sin(\theta) \cdot d\theta) \mathcal{M}_i(j,k) \tag{13}$$

where $N_{pix}(i)$ is the number of pixels enlightenned by the infinitesimal surface i and $\mathcal{M}_i(j,k)$ is a mask equal to 0 if the pixel (j,k) is impacted or 1 if it is not impacted by the scattered light.

Optical component	Distance from OAP-1 (mm)	Diameter (mm)	Beam diameter on reflectors (mm)	OAP focal length
OAP-1	0	30	16.5	900
Tip-Tilt	592	8.23	8.23	/
DM1	952	8.23	8.23	/
OAP-2	1599	30	8.23	902
DM2	2762	30	2.37	/
Parabola-1	3404	30	8.23	902
DM3	4297	8.23	8.23	/
Parabola-2	5191	30	8.23	893
OAP-3	6997	30	8.23	893
Lyot-Stop	7906	6.5	/	/
OAP-4	8407	30	6.5	500
Detector	8907	16	/	/

Table 1: THD2 bench parameters.

Concretely, we calculate for one optical component the total distribution of energy scattered for a set of points from the center of the optical axis to the end of the beam and we spread the resulting intensity with a rotation in all the directions around the image central point. To estimate the contrast level of the scattered light, that image is eventually

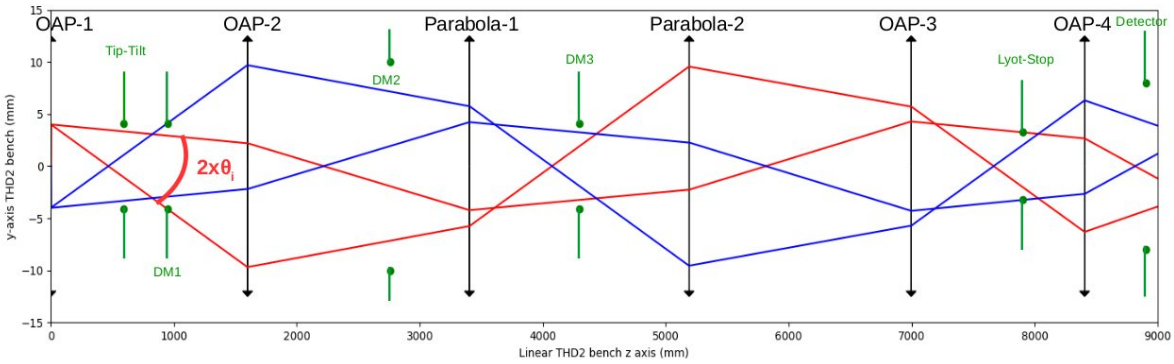

Figure 8: Extreme optical paths calculating by geometrical optics for 2 infinitesimal surfaces located on the OAP-1 (red and blue). Those plots enable to find the light dispersion of each surfaces in the final detector plane.

divided by the maximum of the Airy disk created by an incident beam of intensity E_0 and diffracted by the Lyot-stop (Figure 9). The curve in Figure 9 on the right shows the estimated limitation from scatter for each THD2 mirror except OAP-4 because it is located after the coronograph (E_0(OAP-4) is really weak). We can observe that the most limiting mirror comes from the 2^{nd} deformable mirror location. This was expected because this mirror is really close to a focal plane (Figure 1). Yet, if we sum all those limitations, we find out that the total level is higher than what we get on the THD2 bench (few 10^{-8}).

Some reasons can be given to explain this inconsistency. First of all, we saw in section 3.2 that the simulated BRDF does not fit properly with the measured BRDF at large angles and we need to divide it by a factor between 2 and 3 to match with reality. Moreover, the PSD enable to constrain properly the $\mathcal{B}$ parameter which brings about an overestimation of the Total Integrated Scatter and the BRDF maximum could be reached for larger angles than what we simulated. Eventually, part of the scattered light may be coherent with the specular beam and could be minimized by the {wavefront sensor+ coronagraph} system we use on the THD2 bench[6]. Thus, we continue the study to understand ore in details the amount of scattered light in our experiment.

4. CONCLUSION

In this paper, we measured the level of scatter for an Off-Axis Parabola at large angles. We then used a model to estimate the scattered intensity due to microroughness at narrow angles using the power spectral density of the surface OAP and we found out a consistency between the two independant measures. We use those results, assuming the same scattering behaviour for all the reflectors on the THD2 bench to estimate how scattering impacts the final detector and found that the level of scattered light we estimate is one or two orders of magnitude brighter than the level we measure in the coronagraphic image. Therefore, there is one assumption that is not correct. The BRDF may be overestimated, or the scattered light does not propagate down to the detector as we assume. Nevertheless, this study is a first step to understand how the scattered light impacts the contrast that we can reach on the THD2 bench and the study is still in progress.

ACKNOWLEDGMENTS

The authors would like to thank the Centre National d'Etudes Spatiales (CNES), DIM-ACAV+ and the LABEX ESEP for their financial support. Founded in 1961, the CNES is the french government agency responsible for shaping and implementing France's space policy in Europe. DIM-ACAV+ is a Ile-de-France region funding and support research around Paris in the fields of astrophysics and the conditions for life appearance. ESEP (http://www.esep.pro) is the French acronym of Exploration Spatiale des Environnements Planétaires, or Space Exploration of Planetary Environments whose main strategic goal is to foster R&D projects for new space instrumentation.

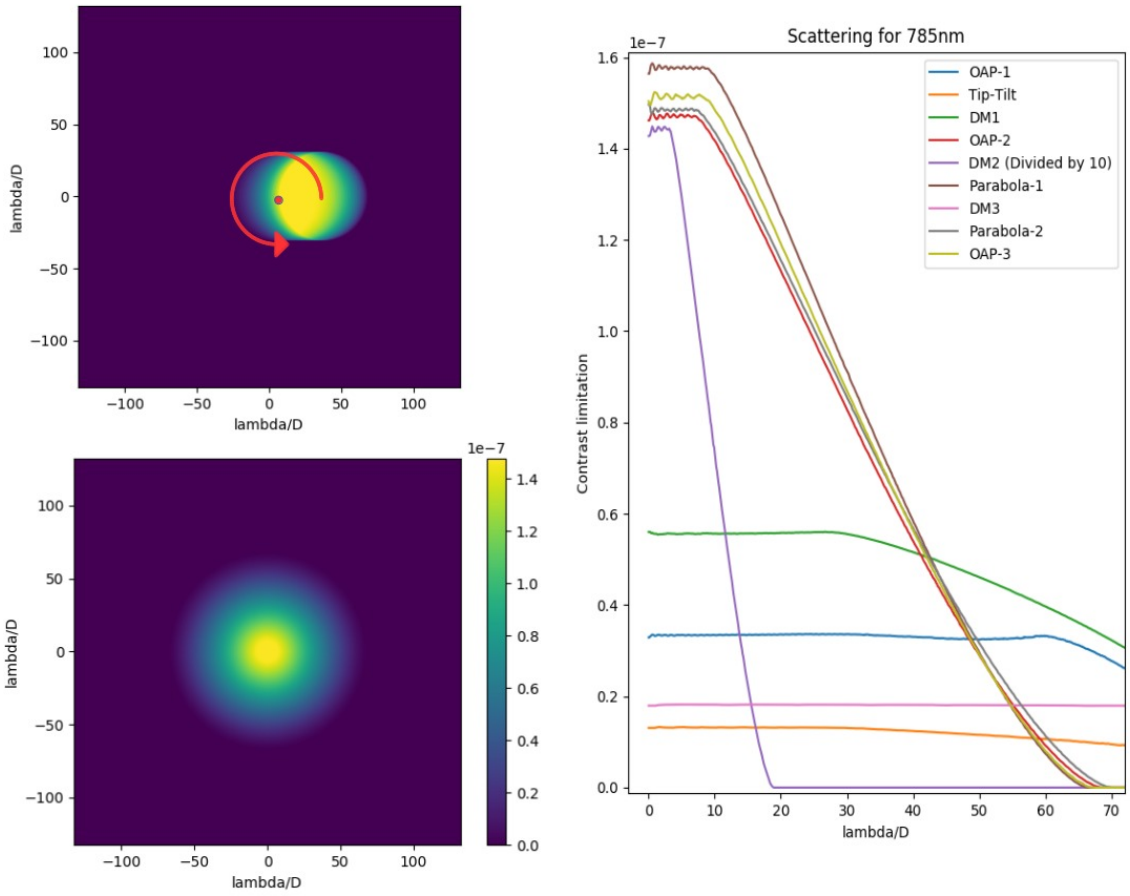

Figure 9: Left, up: total energy scattered for a set of points from the center of the optical axis to the end of the OAP-2 incident beam. The intensity on those pixels are then diluted by rotation around the center of the detector to get the OAP-2 scattering image on the THD2 final detector, normalized by the THD2 incident beam intensity (Figure Left, bottom). On the right, radial plot of those images for all the reflectors. The DM2 contrast limiting effect is divided by 10 for a better vizualization on this graph.

References

[1] Delorme, J., Galicher, R., Baudoz, P., Rousset, G., and Mazoyer, J., "High-contrast imaging in wide spectral band with a self-coherent camera and achromatic coronographs," *Proc. SPIE* **9151** (2014).

[2] Mazoyer, J., Baudoz, P., Galicher, R., and Rousset, G., "High contrast imaging in polychromatic light with the self-coherent camera," *Proc. SPIE* **9151** (2014).

[3] Baudoz, P., Galicher, R., Patru, F., Dupuis, O., and Simone, T., "Status and performance of the THD2 bench in multi-deformable mirror configuration," *AO4ELT* (2018).

[4] Galicher, R., Baudoz, P., Delorme, J., Mazoyer, J., and Rousset, G., "High contrast imaging on the THD bench: progress and upgrades," *Proc. SPIE* **9151** (2014).

[5] Spyak, P. R. and Wolfe, W. L., "Scatter from particulate-contaminated mirrors. Part 1,2,3 and 4," *Proc. SPIE* **Optical Engineering 31**, 1746–1784 (1992).

[6] Balasubramanian, K., Shaklan, S., and Give'on, A., "Stellar coronograph performance impact due to particulate contamination and scatter," *Proc. SPIE* **7440** (2009).

[7] Harvey, J. E. and Anita Kotha, T., "Scattering effects from residual optical fabrication errors," *Proc. SPIE* **2576**, 155–174 (1995).

[8] Harvey, J. E. and Vernold, C. L., "Transfer function characterization of scattering surfaces revisited," *Proc. SPIE* **3141**, 113–127 (1997).

[9] Harvey, J. E., "Light-scattering characteristics of optical surfaces," *PhD Dissertation, Univ. of Arizona* (1976).

[10] Harvey, J. E., Choi, N., and Krywonos, A., "Calculating BRDFs from Surface PSDs for Moderately Rough Optical Surfaces," *Proc. SPIE* **7426** (2009).

[11] Krywonos, A., Harvey, J. E., and Choi, N., "Linear systems formulation of scattering theory for rough surfaces with arbitrary incident and scattering angles," *JOURNAL of the OPTICAL SOCIETY OF AMERICA* **28,6**, 1121–1138 (2011).

[12] Pfisterer, R. N., "Approximated Scatter Models for Stray Light Analysis," *OPN Optics and Photonics News* , 16–17 (2011).